

Dynamical changes of seismic properties prior to, during, and after 2014-2015 Holuhraun Eruption, Iceland

Maria R.P. Sudiby¹, Eva P.S. Eibl¹, Sebastian Hainzl^{1,2}, and Matthias Ohrnberger¹

¹University of Potsdam, Institute for Geosciences, Karl-Liebknecht-Str.24/25, Potsdam-Golm, Germany

²GFZ German Research Centre for Geosciences, Telegrafenberg, 14473 Potsdam, Germany

Correspondence: Maria R.P. Sudiby (pujastutisudiby@uni-potsdam.de)

Abstract. ~~In volcanic eruption monitoring, it is urgent to promptly detect changes in the volcanic system during the crisis period. Ideally continuous, temporally high-resolution, multidisciplinary data is available for this. However, some volcanoes are only being monitored using~~ When a volcano is monitored using only a single discipline or a single seismic station. ~~In this case, it makes sense,~~ it becomes important to harvest information from the ~~available~~ limited data set ~~with several different~~ techniques. Changes in the seismic complexity could reveal ~~the dynamic changes~~ a dynamic change due to magma propagation. We ~~tested the performance of~~ evaluated Permutation Entropy (PE) and Phase Permutation Entropy (PPE) ~~;~~ which are to monitor the 2014-2015 Holuhraun eruption in Iceland. These methods provide fast and robust quantification of time series complexity; ~~to monitor the change in the eruption process of 2014-2015 Holuhraun in Iceland.~~ We additionally calculated the instantaneous frequency (IF), which is commonly used to monitor the frequency changes in a non-stationary signal, root-mean-square (RMS), and root-median-square (RMeS) of the seismic amplitude. We observed distinct changes in the temporal variation of PE, PPE, and IF, which are consistent with the changing state from quiescence to magma propagation and then to eruption. During the eruption, PE and PPE fit the lava discharge rate, showing their potential to forecast the duration of the eruption. ~~Finally, we also assessed the influence of~~ While one parameter may be more sensitive to one stage, the ~~atmospheric noise to be considered in eruption monitoring~~ other may respond better to another stage. Therefore combining them may provide more reliable information. Cluster analysis of these combined parameters shows clusters consistent with the expert interpretation, confirming the power of these parameters in distinguishing different eruption stages.

Copyright statement. TEXT

1 Introduction

A volcano should be monitored using at least four to six seismic stations (Wassermann, 2012; Saccorotti and Lokmer, 2021; Moran et al., 2008). Yet, many volcanoes are only being monitored by fewer seismic stations (Thompson et al., 2015). Monitoring a volcano using one seismic station hinders the classification of the recorded volcano-seismic signals and their location. However, it provides the opportunity to monitor the temporal evolution of both transient and continuous seismic features, which

can give an overview of the state of a volcano. Furthermore, when a volcano observatory starts operating with a single seismic station and only more seismometers are added later, seismic analysis on a single station is important to establish a continuous baseline of monitoring.

An example of single-station monitoring is by estimating the temporal change of seismic velocity (dv/v), which can be influenced by magma intrusion, using ambient noise interferometry (Brenguier et al., 2008). Ambient noise interferometry can be applied to data from a single station either by using cross-component correlation (De Plaen et al., 2016) or by autocorrelation (De Plaen et al., 2019). As a volcanic state can change quickly in a crisis, a high temporal resolution of monitoring is crucial to do a short-term prediction. The estimation of dv/v can be done in a short-time window, such as ~~an hourly window or even~~ minutes, however it requires a dense network ~~is required to achieve an accurate high temporal resolution (Illien et al., 2023). It should also be considered also that~~ (Illien et al., 2023). The dv/v changes ~~do not necessarily also do not always~~ relate to magma intrusions, as the physical properties of the crustal rocks can also be influenced by atmospheric pressure and temperature (Hillers et al., 2015), changes in ground water level (Sens-Schönfelder and Wegler, 2006), and ground freezing (Steinmann et al., 2020).

Entropy is a term that is broadly used to measure a level of disorder of a system, e.g. in thermodynamics (Cropper, 1986), statistical mechanics (Wehrl, 1978), and information theory (Shannon, 1948). In nature, a state that is not balanced will always shift to reach equilibrium, and this process can be associated with increasing entropy (Posadas et al., 2023). In seismology, increasing entropy can be related to the irreversible transition of unbalanced stress and strain in the crust, culminating in earthquakes (De Santis et al., 2011; Posadas et al., 2021, 2023). The changes in entropy can be linked to earthquakes' seismic cycle (Posadas et al., 2023), where the entropy increases and reaches its maximum value at or shortly after the main shock, followed by a drop and then stabilizes during the relaxation period (De Santis et al., 2011; Posadas et al., 2021, 2023).

One of the methods to estimate entropy using the amplitude of a time series is Permutation Entropy (Bandt and Pompe, 2002). Glynn and Konstantinou (2016) calculated Permutation Entropy (PE) based on seismic time series to find a precursor prior to 1996 Gjalp eruption in Iceland. In principle, PE is estimated using one station. When several stations are available, PE can be estimated from them to verify whether its temporal evolution is consistent at all stations. During the propagation of magma to the surface, magma will interact with the varying surrounding rocks at depth and create different seismic signals with different complexities. As magma reaches the surface, magma interaction with the shallow subsurface can generate tremor and/or long period signal. When a pre-eruptive tremor and/or long period signal is present, they exhibit a more regular oscillation and are narrow banded in frequency, and hence PE is reported to drop (Konstantinou et al., 2022).

While PE can detect a seismic precursor occurring days before an eruption (Glynn and Konstantinou, 2016), PE is also reported to be sensitive to detect fast changes. Sudibyo et al. (2022) calculated PE for 63 eruptions of Strokkur geyser in Iceland where the duration of a typical eruptive cycle is 3.7 ± 0.9 min (Eibl et al., 2020). The PE can resolve the typically observed four phases of Strokkur's eruptive cycle, that last several seconds to several minutes (Eibl et al., 2021), and 1 s long processes therein at high resolution (Sudibyo et al., 2022).

Apart from the amplitude, another useful property of the continuous seismic recording is the phase information. Instantaneous phase, along with the other seismic attributes, has been utilized in seismic reflection to map geological discontinuities in

shallow subsurface since the 1970s (Taner et al., 1979). In seismology, the instantaneous phase has been used e.g. in seismic tomography (Bozdağ et al., 2011) and noise suppression in ambient noise cross-correlation (Schimmel et al., 2011; De Plaen et al., 2019). Kang et al. (2021) introduced the use of the instantaneous phase to calculate Phase Permutation Entropy (PPE), which is also shown to be sensitive towards dynamic changes of a signal. Here we use the application of PE and PPE in detecting the dynamic changes before, during, and after the Holuhraun eruption 2014-2015, Iceland.

Different observable parameters from various methods are required to form a robust forecasting framework. Understanding which parameters to use and how they can represent the process in the system can help improve the framework's accuracy and reduce the computational cost. Here we also assess the derivative of the instantaneous phase, which is known as instantaneous frequency (IF) (Boashash, 1992) which is commonly used to do time-frequency analysis for a non-stationary signal.

From 16 August 2014 seismicity migrated for two weeks from subglacial Bárðarbunga volcano in North-East Iceland, first to the southeast, then to the northeast for about 48 km, at a depth of 5 to 9 km (Ágústsdóttir et al., 2016, 2019). This seismicity is interpreted as induced by a dike intrusion which is divided into 4 segments S1 to S4 (Woods et al., 2019), and culminated in an eruption that formed the Holuhraun lava flow field (see Figure 1a and b). Along the dike path, three cauldrons formed on the ice surface, possibly indicating small subglacial eruptions (Eibl et al., 2017b; Reynolds et al., 2017). After the dike reached Holuhraun, a short-lived eruption occurred during the night on 29 August 2014 and was followed by a 6-month-long eruption from 31 August 2014 at the same site. Another subglacial eruption possibly occurred on 3 September 2014 (Eibl et al., 2017b) and another subaerial eruption took place from 5 to 7 September 2014 between the ice cap and the main lava flow field (Pedersen et al., 2017; Eibl et al., 2017a). The spatial chronology is shown in Figure 1a, while the chronology timeline is shown in Figure 1b.

This 2014/2015 Holuhraun eruption is exceptionally well monitored by combining a variety of disciplines. In terms of eruption forecasting this eruption is interesting due to several subglacial eruptions, three subaerial eruptions and the extensive dike formation. In addition, a dense network of 72 seismometers (Woods et al., 2018) was distributed around the growing lava flow field providing a wealth of data. The lack of recorded shallow seismicity prior to the eruptions (Sigmundsson et al., 2015) raises a question whether the final magma movement is aseismic or generates pre-eruptive tremor as suggested by Eibl et al. (2017b).

In this paper, we first introduce the PE (section 2.2) and the PPE method (section 2.3), along with other ~~quantifications~~ quantification consisting of Instantaneous Frequency (IF) ~~, RMS and RMeS, and TADR~~ (section 2.4), Root-Mean-Square (RMS) and Root-Median-Square (RMeS) of seismic amplitude (section 2.5), the Time Average Discharge Rate (TADR) (section 2.6), and K-means clustering (section 2.7). Synthetic tests to evaluate the performance of PE and PPE are provided in section 3.1. Additionally, we provide an explanation of the parameters utilized to calculate PE and PPE (section 3.2) as well as IF, RMS and RMeS (section 3.3). We then compare the temporal variation of PE, PPE, IF, with the RMS of seismic amplitude and the hypocentral distances to the station (section 4). Furthermore, we discuss the temporal variation of PE, PPE, and IF during the repose time (section 5.2), during the dike propagation (section 5.3) and ~~eruptive time~~ the eruption (section 5.4). During ~~the eruptive time eruption~~, we compare them with the ~~calculated~~ lava effusive rate ~~Coppola et al. (2017)~~ (also section 5.4). We show the clustering of PE, PPE, ~~and IF~~ IF and log(RMeS) in section 5.5, before we provide our ~~conclusions~~ conclusion.

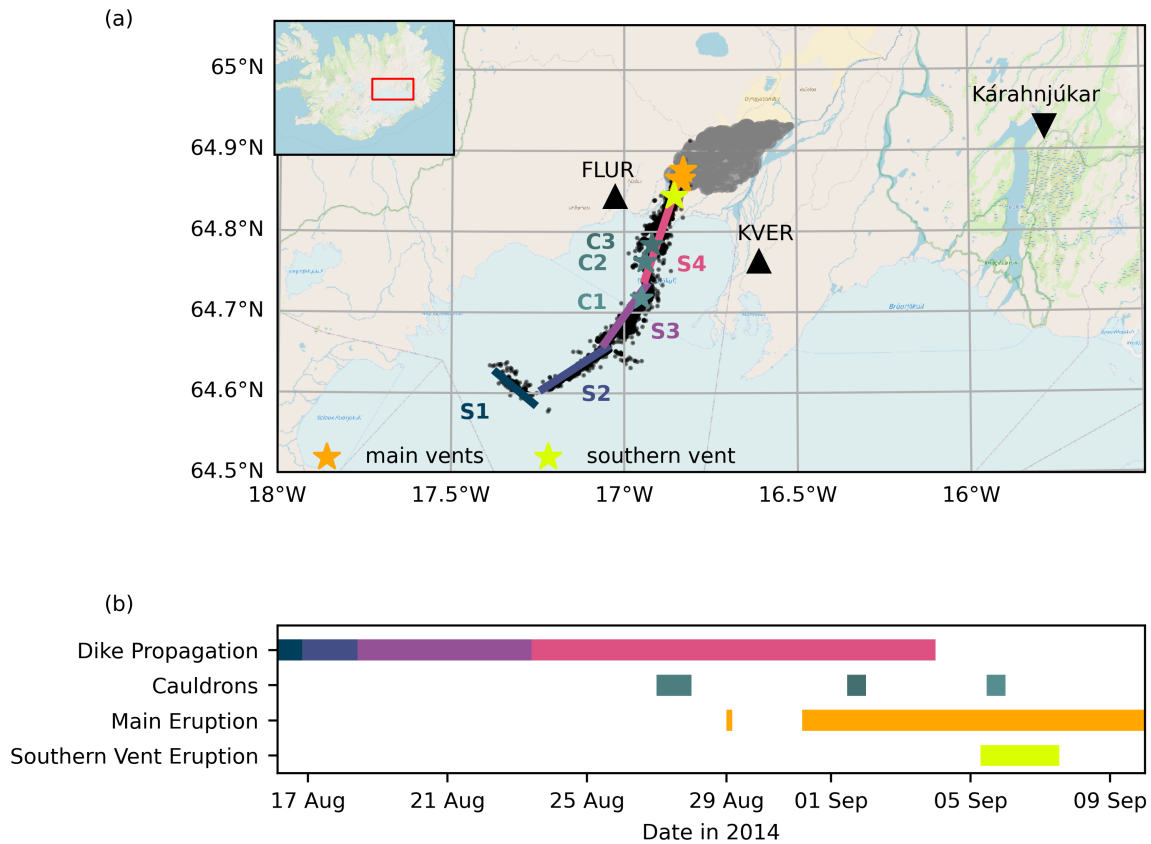


Figure 1. Overview of the unrest followed by the 2014/2015 Holuhraun eruption, Iceland. (a) The recorded earthquakes from the catalog of Ágústsdóttir et al. (2019) are represented by the black dots, the activated dike segments (lines; S1 to S4) as reported by Woods et al. (2019), the erupted lava flow field (gray shaded area) from Voigt et al. (2021), the location of seismic station FLUR and KVER (black triangles) and the weather station at Kárahnjúkar (black inverted triangles). (b) The temporal information of the dike propagation (Woods et al., 2019), observation of the cauldrons (Eibl et al., 2017b; Reynolds et al., 2017), the main eruption and the southern vent eruption (Eibl et al., 2017a).

2 Method

2.1 Seismic network

95 A dense seismic network (network code Z7) was maintained in the area of the Holuhraun 2014-2015 eruption (White, 2010). 50 stations were running long enough to record the seismicity from the first half of 2014 to the end of 2015. Based on its proximity to the dike and eruption vents and data availability, we chose station FLUR for further analysis. This station is located about 32.7 km north of Bárðarbunga and about 9.1 km southwest of the Holuhraun lava flow field. At FLUR, a Guralp CMG-3ESP broadband sensor recorded at a frequency sampling of 100 Hz. For comparison, we used station KVER which is located about 100 14 km southeast of the lava flow field. At KVER, a Guralp CMG-6T broadband seismometer recorded at 100 Hz sampling rate. The location of these two stations is shown in Figure 1a.

2.2 Permutation Entropy (PE)

PE quantifies the probability distribution of ordinal patterns in a time window. An ordinal pattern is a vector representing the relative order of the amplitudes. For example, a sequence of {0.32, 1.0, 2.7, 3.5, 5.0} is represented by the ordinal pattern of {0, 105 1, 2, 3, 4}, while {3.1, 2.2, 1.1, 3.8, 5.0} is represented by {2, 1, 0, 4, 5}. To reconstruct an ordinal pattern, we downsample the time series using an embedding dimension m and a delay time τ . The embedding dimension m is the total number of samples in the sequence, and the delay time τ is the time gap between samples. The vector of the ordinal pattern is first constructed by $[x_s, (x_s + \tau), \dots, (x_s + (m - 1)\tau)]$. The next ordinal patterns then are reconstructed by shifting x_s one sample forward, continuously until the last ordinal pattern reaches the end of the window.

110 Then, we calculate PE as:

$$PE = \frac{-1}{\log m!} \sum_{k=1}^{m!} p_k \log p_k \quad (1)$$

where p_k is the probability of the ordinal pattern k . p_k is determined by the relative frequency N_k/N , where N_k is the number of patterns k observed in the window, and N total number of ordinal patterns in the window. Equation 1 is then normalized by the maximum number of different ordinal patterns $\log m!$, leading to a PE between 0 and 1.

115 An example of the PE calculation is illustrated in Figure 2. Subfigure 2a shows a 5-hour-long seismic time series recorded by the vertical component at station FLUR, Iceland. This seismic waveform has been bandpass-filtered between 0.5-10 Hz. We first divided the time series into 1 hour long windows without overlap. We then used $m = 7$ and $\tau = 0.04$ seconds to reconstruct the ordinal patterns (Figure 2b). Note that the τ used in Figures 2 is for the illustration purpose while the real analysis in this paper uses parameters mentioned in Section 3.2. Finally, in each 1 h window, we calculated its respective PE (Figure 2e).

120 2.3 Phase Permutation Entropy (PPE)

A seismic time series, denoted as $x(t)$, can be regarded as the real component of the seismic analytic ~~trace~~ $X(t) = x(t + iy(t))$ signal $X(t) = x(t + iy(t))$, where $y(t)$ is the imaginary component obtained by applying the Hilbert transform to $x(t)$ (Gabor, 1946;

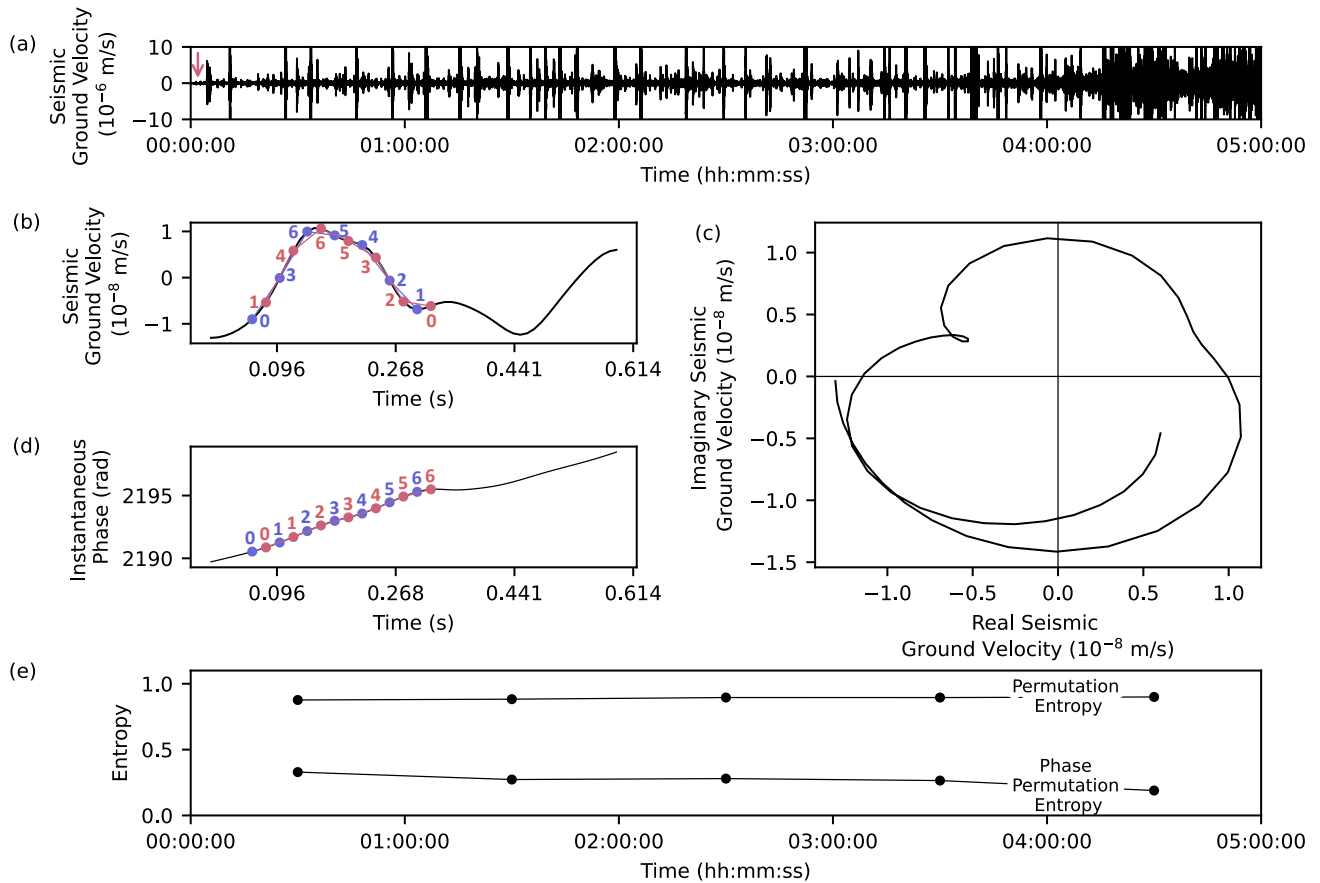


Figure 2. The overview of PE and PPE calculation. (a) Five hours of seismic time series from the vertical component of FLUR station, filtered between 0.5-10 Hz. (b) The amplitude of the waveform starting at the red arrow in subfigure (a) with two consecutive ordinal patterns $\{0, 3, 6, 5, 4, 2, 1\}$ and $\{1, 4, 6, 5, 3, 2, 0\}$. (c) The analytic signal reconstructed from the same part of the signal in the complex plane. (d) The unwrapped instantaneous phase of the analytical signal in subfigure (c) with two examples of consecutive ordinal patterns $\{0, 1, 2, 3, 4, 5, 6\}$. Note that the linear trend of the instantaneous phase leads to fewer different ordinal patterns than the seismic amplitude data. (e) The estimated PE and PPE for the waveform in subfigure (a).

Taner et al., 1979; Barnes, 1992). The Hilbert transform is an equivalent of a linear filter, where the amplitudes of a signal are unchanged but their phases are shifted by $-(\pi/2)$ (Feldman, 2011). Scipy is a free and open source Python library (Virtanen et al., 2020) that provides a tool to compute the analytic signal from a [real signal time series](#). The function of `scipy.signal.hilbert` implements the step defined by Gabor (1946) in computing an analytic signal $X(t)$, as followed:

1. Fourier transforming the real component,
2. zeroing the amplitude for negative frequencies and doubling the amplitude for positive frequencies,
3. inverting Fourier transform.

130 The instantaneous phase can be defined as the degree of the $X(t)$ rotation. The instantaneous phase $\theta(t)$ is calculated using

$$\theta(t) = \tan^{-1} \left(\frac{y(t)}{x(t)} \right). \quad (2)$$

PPE is introduced by Kang et al. (2021) to calculate a wave's complexity using the instantaneous phase of an analytic signal. In calculating PPE, we reconstruct the ordinal pattern using the instantaneous phase which is obtained from equation 2. Unlike Kang et al. (2021) who used the wrapped instantaneous phase from $-\pi$ to π to construct the ordinal pattern, here we use the
 135 unwrapped instantaneous phase. For a reference, a sine wave will have a linear increase of unwrapped instantaneous phase, producing only one ordinal pattern. Its respective PPE value hence is 0.

An example of PPE calculation for a seismic time series (Figure 2a) is shown in Figures 2c, d, and e. We first obtain the analytic signal (Figure 2c). We then estimate the instantaneous phase and reconstruct the ordinal patterns (Figure 2d). Finally, we estimate the PPE from the probability of the reconstructed ordinal patterns (Figure 2e).

140 2.4 Instantaneous Frequency (IF)

The instantaneous frequency (IF(t)) is defined as the derivative of the instantaneous phase $\theta(t)$,

$$IF(t) = \frac{1}{2\pi} \frac{d}{dt} \theta(t) \quad (3)$$

2.5 Root-Mean-Square (RMS) and Root-Median-Square (RMeS) of the Seismic Amplitude

The Root-Mean-Square (RMS), the root of mean squared seismic amplitude, is commonly used in volcano monitoring to
 145 continuously estimate the average seismic energy.

$$RMS = \sqrt{\frac{1}{n} \sum_i x_i^2} \quad (4)$$

In some cases where both volcano-tectonic (VT) events and tremors are present, VT events will dominate the RMS and conceal the tremor in the RMS time series. Calculating the root of median squared seismic amplitude (RMeS) will emphasize the tremor energy more (Eibl et al., 2017a). **In this paper, RMS is calculated during the dike propagation, and RMeS is calculated**

150 ~~during the eruptive period. Both RMS and RMeS~~ are calculated using 1h of window length without overlapping. For x^2 values sorted by size, ~~RMeS~~ RMeS is calculated as follows.

$$RMeS = \begin{cases} \sqrt{x_{(n+1)/2}^2} & \text{if } n \text{ is odd} \\ \sqrt{0.5(x_{n/2}^2 + x_{n/2+1}^2)} & \text{if } n \text{ is even} \end{cases} \quad (5)$$

2.6 Time Average Discharge Rate (TADR)

Coppola et al. (2016) exploited the middle-infrared data acquired by multiple sensors from multiple satellites. These infrared
155 data can be used to identify the thermal radiation emitted by volcanic eruption processes. The intensity of the thermal anomaly is known as volcanic radiative power (VRP). During an effusive eruption, VRP can be used to calculate the time average lava discharge rate (TADR) in m^3/s^1 .

$$TADR = \frac{VRP}{c_{rad}}, \quad (6)$$

where c_{rad} (Jm^{-3}) is the radiant density representing the efficiency of the lava body to modulate the heat.

160 2.7 K-means clustering

K-means is a non-supervised clustering method to find K numbers of clusters, each consisting sets of points which are evenly spaced in a D -dimensional Euclidian space (Bishop, 2006). The D - dimension is determined from the D numbers of seismic parameters used. We describe the data set of each seismic parameter as $x_n = X_1, \dots, X_N$. The steps on assigning each data points of D seismic parameters into K clusters is elaborated as follows. We introduce an initial set of D -dimensional vectors μ_k which represent the center of the cluster k , where $k = 1, \dots, K$. We then need to find an assignment, so that the sum of the squares of the distances (J) of the data points X_1, \dots, X_N to its closest vector μ_k is minimum.

$$J = \sum_{n=1}^N \sum_{k=1}^K r_{nk} \|x_n - \mu_k\|^2 \quad (7)$$

where $r_{nk} = 1$ if the data points x_n are assigned to cluster k and $r_{nk} = 0$ if otherwise.

To find the values of r_{nk} and μ_k where J is minimum is done by iteration using three successive steps. Initially, we choose randomly the initial value of μ_k . Second, we minimize J with respect to r_{nk} while keeping a fix μ_k . Then, we minimize J with respect to μ_k while keeping r_{nk} fix (Bishop, 2006).

2.8 Weather data

A weather station located in Kárahnjúkar, about 59.7 km from the FLUR station (Figure 1a), provides weather data as a reference for the analysis during the repose time. The station was installed at 639 m above sea level and measures 10 m above
175 the Earths surface. ~~For every hour, it samples the~~ It measured the average of the last 10 minutes ~~of~~ wind speed and the last 1 minute ~~of temperature, then calculates their average value~~ temperature. The data is provided by the Icelandic Meteorological Office and is available by email request.

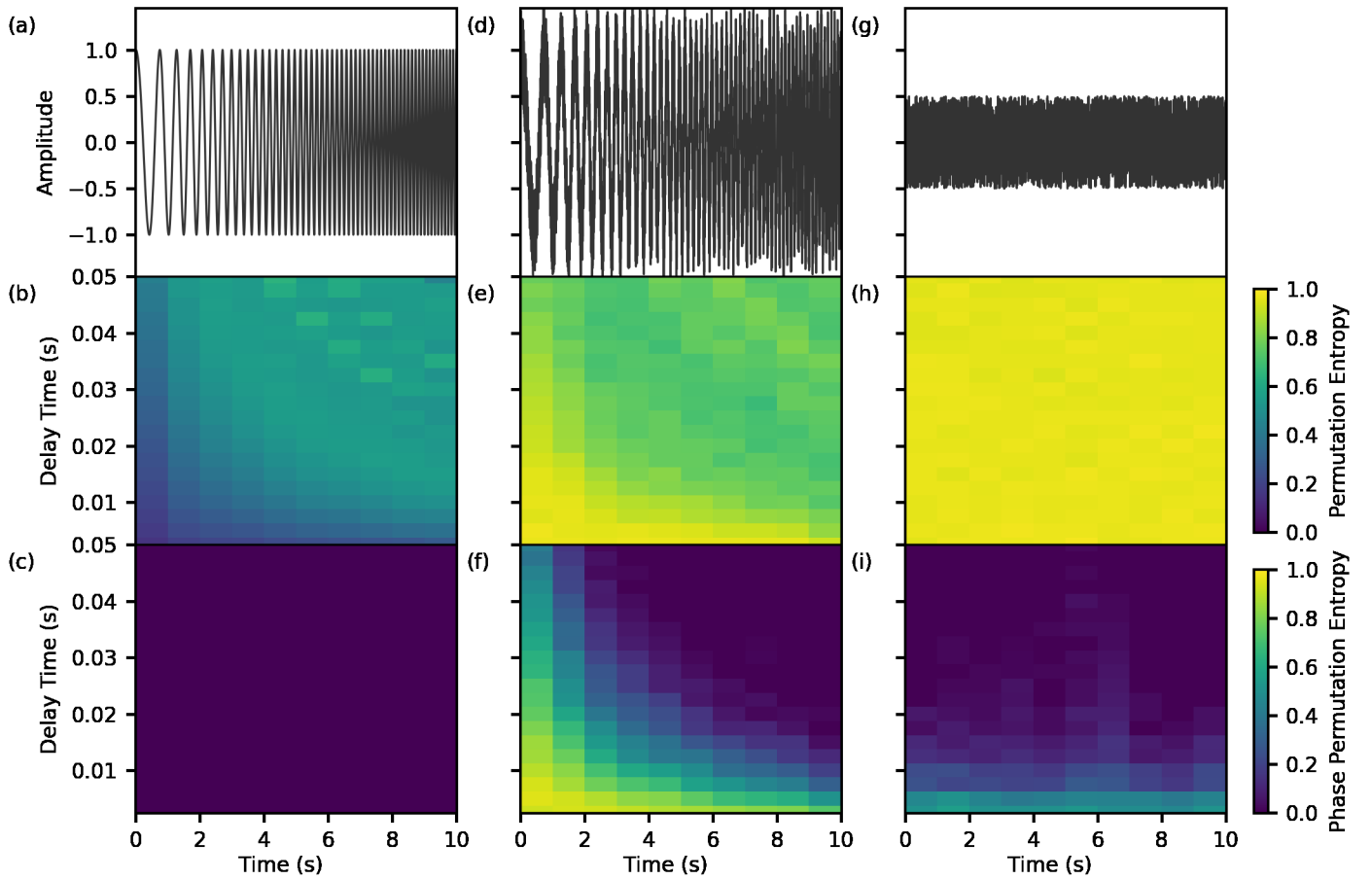


Figure 3. Synthetic test (a) time series of a chirp signal, (b) PE and (c) PPE. (d-f) Same as subfigures (a-c) for a noisy chirp signal. (g-i) Same as subfigures (a-c) for noise.

3 Synthetic test and the application to seismic data

3.1 Synthetic tests

180 Sudibyo et al. (2022) tested different delay times τ to obtain optimum PE for stationary signals with different bandwidths. For a noisy stationary signal, PE is less affected by noise when τ is not too small nor equal to the fundamental period. τ is related to the frequency of the signal. When the frequency of a non-stationary signal changes, it will influence the calculated PE as the calculation uses a fix τ . This behavior was not investigated in detail in the previous study.

Here we investigated the differences in PE and PPE calculation on three different synthetic signals. First, we generated a
 185 chirp signal with increasing frequency from 1 to 10 Hz and a sampling rate of 400 Hz (Figure 3a) and then added a demeaned

uniform noise (Figure 3d). Furthermore, we also tested the noise itself (Figure 3g). We used the Numpy library (Harris et al., 2020) to create the chirp signal and the noise, and then calculated their PE and PPE for every 1s-window length. We use $m = 5$, which is the highest m possible to calculate PE and PPE based on the number of samples for 1s window length.

In this test, we focus on how a changing frequency could affect the PE and PPE calculation. We tested different τ from the shortest possible to 0.5 s, which is the Nyquist period of the high-frequency corner of the signal. Figures 3b and e show that using $\tau > 0.25$ s, which is half of the Nyquist period, generates artifacts in PE of the higher frequencies. Figure 3b shows that the PE of the chirp signal increases when the frequency increases. This is due to the less repeating ordinal patterns reconstructed when the frequency increases. An opposite behavior is shown in Figure 3e for the noisy chirp. Noise increases the PE (Figure 3h). Due to the fix τ , the ordinal pattern samples relatively more noise at lower frequencies. When the frequency increases, the length of the ordinal patterns get closer to the signal's wavelength and the signal-to-noise ratio increases, resulting in a lower PE at higher frequency.

PPE utilizes the instantaneous phase. The ~~unwrap~~-unwrapped instantaneous phase of a chirp signal is always increasing (Figure S1a), producing only one ordinal pattern, resulting in PPE=0. In the case of the noisy chirp, the noise contains non zero-crossing amplitude and generates tangled rotation in its analytical signal as shown in Figures 2c, and S1f and j. These tangled rotations have decreasing phase angles which generate different ordinal patterns (Figures S1h and i), hence increasing PPE.

A common practice to reduce noise and isolate the signal of interest is by filtering. We tested how PE and PPE change if a noise gets filtered. Figure S2 shows a decrease in PE and PPE in the filtered noise, with wider bandwidth possessing higher PE and PPE than a narrower bandwidth.

205 3.2 Parameter selection in calculating PE and PPE of seismic time series

The parameters required to calculate PE and PPE are window length, embedding dimension m , and delay time τ . To determine the window length, we need to fulfill two requirements, the minimum number of samples required by the embedding dimension m and the targeted resolution in the temporal variation of PE and PPE. To calculate PE and PPE, the number of samples in a window has to be more than $m!$, where $m!$ is the maximum number of possible ordinal patterns reconstructed from the embedding dimension m . In the case of a noisy signal, it is advised to use window length longer than 5! (Amigó et al., 2008) to cover all possible patterns generated by the noise. Following the suggestion, for $m = 7$ we need a minimum sample of 25200 points or equal to 252 seconds. As seismic precursors can range from hours to days prior to an eruption, we chose 1 hour of window length which also fulfills the requirements of the number of samples needed by the mentioned embedding dimension. The delay time τ needs to be smaller than the Nyquist period of the targeted signal (Berger et al., 2017), and our synthetic test recommends $\tau < 0.5$ Nyquist period. Our interest lies in frequency between 0.5 to 10 Hz. Tremor is found to be between 0.8 to 2.5 Hz (Eibl et al., 2017b) and we found regular repeating noise at frequencies above 10 Hz. The Nyquist period for a 10 Hz signal is 0.05 s, and we chose $\tau = 0.02$ s.

We processed 2 years of seismic data recorded at the vertical component of station FLUR from January 2014 to December 2015, covering the repose period, the unrest and the eruption. We used Obspy to read the seismic data and to apply a But-

220 terworth bandpass filter of order 4. A Butterworth filter does not create ripples in the pass-band, which is important to avoid artificial ordinal patterns. We activated the option zero-phase in the Butterworth filtering, to obtain no phase shift in the filtered seismogram. All plotting is done using Matplotlib. A comparison between the two stations, FLUR and KVER, shows similar temporal variations of PE and PPE in both stations (Figure S3).

3.3 Calculation of IF, RMS, and RMeS

225 We also used the vertical component of FLUR for the IF, RMS, and RMeS calculations and adapted the same 0.5-10 Hz frequency band used for the IF calculation. First, we estimated the Instantaneous Phase for every seismic data sample and then we calculated IF from every two consecutive Instantaneous Phases. We then calculate the mean IF for every 1h window, to obtain the same resolution as PE and PPE. [In this paper, we refer the hourly mean IF as IF.](#) The calculation of RMS and RMeS also uses the same 1h window length, and within the frequency from 0.5 to 10 Hz.

230 3.4 [Parameters selection in K-means Clustering](#)

[We performed a clustering analysis to assess the capability of the calculated seismic parameters to discriminate the different processes before and during the eruption. We used PE, PPE, and IF to generate a 3D Euclidian space, and added RMS or RMeS to generate a 4D Euclidian space. The lava discharge rate is not used in the clustering since it is only available during the eruption. We generated three clusters representing the major events: quiescence, dyke propagation, and eruption in these spaces using Scikit-Learn \(Pedregosa et al., 2011\). To validate the result, we also clustered the data based on the timeline of the eruption processes consisting of \(i\) quiescence, \(ii\) the propagation of four dyke segments \(Woods et al., 2019\), \(iii\) the presumed sub-glacial eruption \(Eibl et al., 2017b\) and the subaerial eruption \(Eibl et al., 2017a\). We then calculated how many points in clusters by the expert interpretation fall into the equivalent K-means clusters and normalized them by the total points in each interpreted clusters. This quantification is expressed in the confusion matrix. By choosing the confusion matrix with the highest score, we can choose the best clustering result. The resulting confusion matrix for different combination of seismic parameters is shown in Table S1 to S5.](#)

235
240

4 Results

In the following, we will describe the temporal variation of various features of the seismic waveform in the last 5 days of the repose time, the 14 days of earthquake migration, and the first 15 days of the main eruption (Figure 4). We will also describe the further evolution until March 2015 when the eruption ended (Figure 5).

245

4.1 The earthquakes hypocentral distances and RMS of seismic amplitude

More than 30,000 earthquakes are listed in the earthquake catalog by Ágústsdóttir et al. (2019). They migrate from the southeastern rim of subglacial Bárðarbunga volcano at 29-32 km distance and then progress to the Holuhraun lava field at about 8-12 km distance from station FLUR (Figures 1a and 4a). The dike segments S1 to S4 (Woods et al., 2019) feature distinctly

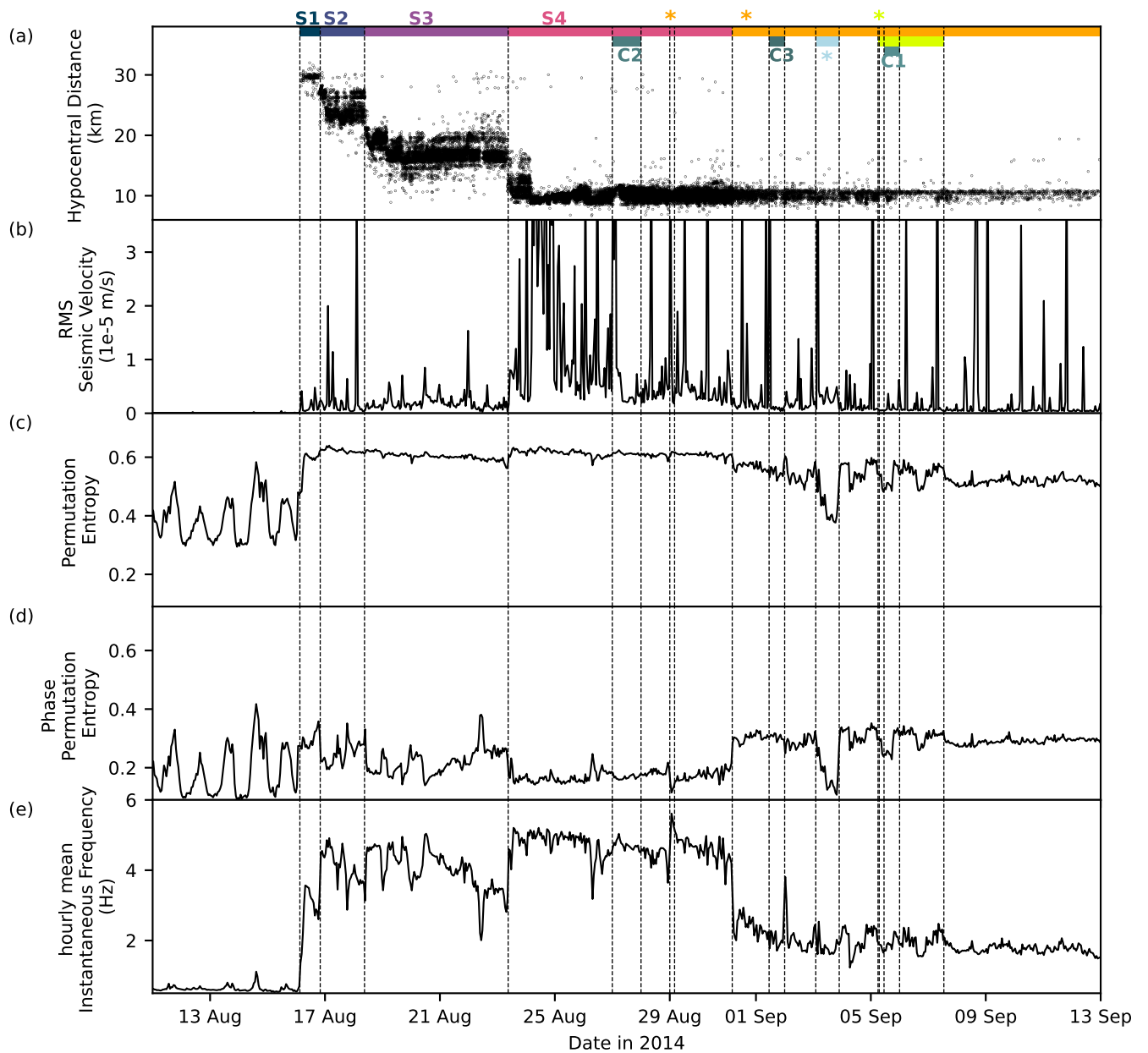


Figure 4. Overview of the seismic characteristics during the quiescence, eruption preceding seismicity, and the first 15 days of the eruption: (a) hypocentral distances of the earthquakes to the FLUR station, (b) RMS, (c) PE, (d) PPE, and (e) $\overline{\text{mean-IF}}$. RMS, PE, PPE, and IF are calculated from seismic time series recorded at the vertical component of station FLUR, filtered between 0.5-10 Hz. The segmentation of the dike (S1-S4, dark blue to pink horizontal lines), cauldrons observed on glacier surface (C1-C3, dark green horizontal lines), tremor on 03.09.2014 interpreted as presumed subglacial eruption (Eibl et al., 2017b) (light blue), eruption from the southern vent (light green horizontal line and light green star) and the main eruption (yellow horizontal and yellow stars) are marked in subfigure (a) and by dashed vertical lines in all panels.

250 different distance ranges. The hypocentral distance to our station decreased quickest at the beginning of each segment when it formed and the distance stalled towards the end of a segment. In segment S3, the earthquakes moved in several episodes, on 18-20 August 2014, and later a short quiescence occurred on 22 August 2014 at 10:00. While in segment S4, the earthquakes kept moving to the northeast, their distances to FLUR remained around 10 km. After the onset of the main eruption on 31 August 2014, the number of earthquakes became fewer and the seismic time series was dominated by eruptive tremor.

255 Consequently, the seismic waveform is not only dominated by earthquakes but also features seismic volcanic tremor. During repose time the RMS is mostly below $5 \cdot 10^{-7}$ m/s. During dike formation, the RMS of the seismic amplitude is very spiky and affected by the earthquakes (Figure 4b). RMS increases significantly after S4 starts on 23 August 2014 and is also dominated by spikes throughout the segment and the eruptive period. During S4, the RMS exhibits few fluctuations from 23-24 August, 24-26 August, 26 August-1 September 2014. During the eruptive period, there is an increase between 2-4 September. Afterward, the
260 RMS amplitude is mostly low and decreases with time with spikes throughout the eruptive period.

4.2 The temporal evolution of Permutation Entropy (PE)

During the repose time, PE displays a strong daily variation (Figure 4c). A sharp increase is observed on 16 August 2014 when the earthquakes occur and start to migrate. PE stays high, mostly above 0.6 during the two weeks of the earthquake migration. Prior to the main eruption on 31 August 2014, PE exhibits three decreasing trends: segment S1 to S2, S2 to S4, and a more
265 gentle slope during S4 to the onset of the main eruption. After the main eruption begins, there is a notable decrease in PE, followed by a strong drop on 3 September 2014, when PE reaches a value of 0.37. The drop on 3 September represents a local minimum that persists for one day. PE then fluctuates between 4 and 7 September and subsequently gets more steady after 10 September 2014. PE generally declines toward the end of the eruption (Figure 5a). The comparison of PE with TADR from Coppola et al. (2017) reveals a similar shape of both (Figure 5a). Note that the TADR is plotted on a log scale, while PE is in a
270 linear scale.

4.3 The temporal evolution of Phase Permutation Entropy (PPE)

Similar to PE, PPE also exhibits a strong daily variation during the repose time (Figure 4d). Interestingly, during the earthquakes migration, PPE follows a pattern that is anti-correlated to that of PE and IF. PPE increases from 0.27 at S1 to 0.32 at S2, but
followed-by-a-drop drops to 0.224 in the next two hours. PPE then drops to 0.14 on 20 August followed by a sharp increase
275 until 23 August 2014. An abrupt drop occurs on 23 August 2014 when the time segment S4 starts, followed by two successive increasing trends which culminate in the eruptions on 29 and 31 August 2014. Before the eruption, another peak is observed on 22 August 2014 at 10:00 and 26 August at 07:00. These peaks occurred one day before the presumed subglacial eruptions on 23 and 27 August 2014. PPE increases abruptly right after the main eruption starts. Interestingly, this is then followed by a pattern that is similar to the pattern in PE. PPE also drops and reaches the minimum value on 3 September 2014 for 1 day
280 and generally declines towards the end of the eruption. The trend observed in PPE also aligns well with the shape of the lava effusion rate (Figure 5b), with PE plotted in a linear scale and TADR in a log scale.

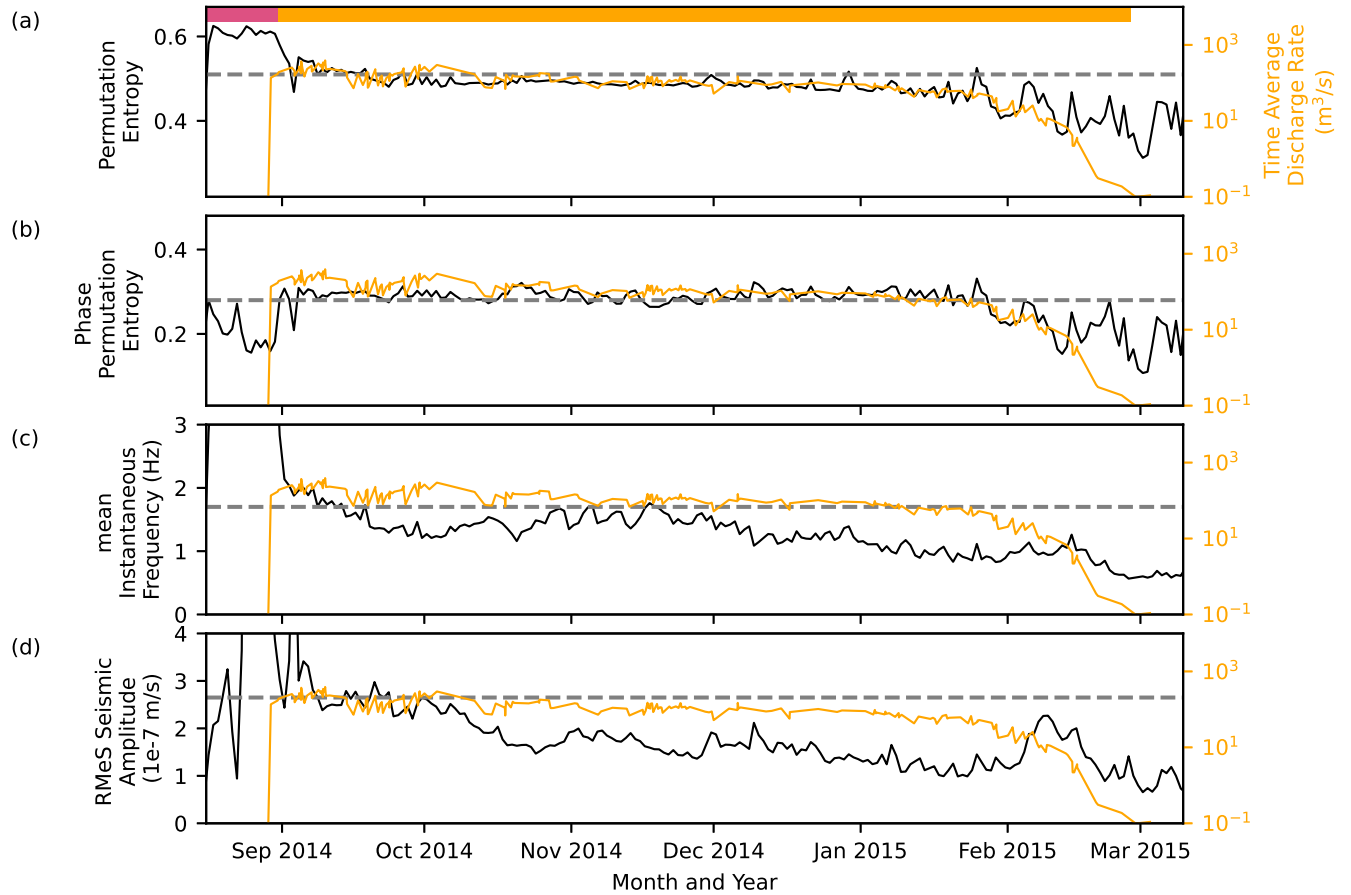


Figure 5. Overview of the 6-month long subaerial eruption. Comparison of (a) PE, (b) PPE, (c) **mean**-IF and (d) RMeS seismic velocity (all black) on a linear y-axis, with lava effusion rate Coppola et al. (2017) plotted on a logarithmic y-axis (orange line, scale on right). Note the different y-scales for PE and PPE. All values were calculated using 1 day window-length. The dashed line marks the reference line, obtained from the value of PE, PPE, IF, and RMeS on 8 September 2014, when the eruption starts to stabilise.

4.4 The temporal evolution of the mean Instantaneous Frequency (IF)

Before the start of the two-week migration of earthquakes, the **mean-IF** is mostly low between 0.5 to 0.8 Hz and exhibits a daily variation (Figure 4e). An abrupt increase in **mean-IF** is observed when the swarm starts on 16 August 2014. IF is generally increasing from 16 to 20 August 2014, with values from 3 to 5 Hz during the propagation of segments S1 to S3. Even though it generally increases, IF exhibits a quasi-periodic fluctuation with each period varying from 4 to 12 hours. There are two decreasing trends within this fluctuation, which fit the time length of segment S1 and S2. IF was the highest at the beginning of both segments and continuous dropping towards the end of the segments. IF is generally higher during S2 than during S1. IF continues to increase from the beginning of S3 for two days before decreasing towards the beginning of S4. During the propagation of S4, IF decreases fast before the onset of the eruption on 29 August and continues a more slow decrease towards the main eruption on 31 August. During the earthquakes' migration, IF is anti-correlated to PPE.

Two sharp drops of IF are also observed at 10:00 on 22 August and at 07:00 on 26 August 2014, at the same time when the two peaks of PPE are observed. Another drop is also observed on 28 August 2014 at 22:00 followed by a sharp increase to the maximum value of 5.6 Hz, marking the onset of the short eruption on 29 August 2014. After the onset of the main eruption on 31 August 2014, IF drops from 4.2 Hz to 2 Hz. IF increases slightly from October to November 2014, then in general decreases to the end of the eruption on 28 February 2015 (Figure 5c).

5 Discussion

5.1 Factors affecting the complexity quantification in PE and PPE

The synthetic tests in subsection 3.1 show that PE, calculated using a fix m and τ , is higher for a signal with higher frequency content compared to one with lower frequencies. A signal with energy in a broad frequency bandwidth usually possesses a high PE (Dávalos et al., 2021; Sudibyo et al., 2022). Independent of its frequency content, PPE is more affected by the presence of non-zero-crossing oscillation in its signal. When a low-frequency signal is superposed with a weaker signal with a higher frequency, most oscillations of the higher-frequency part do not cross zero amplitude. This oscillation type will cause more complex rotation in its analytical signal (Figure S1f), resulting in more ordinal patterns and higher PPE.

5.2 The influence of atmospheric processes on PE, PPE, and **mean-IF**

We investigated the influence of temperature and wind on the hourly PE, PPE, and **mean-IF** during different seasons from 2014 to 2015. Seasonal variation including temperature, wind speed, and air pressure is common to be observed in seismic ambient noise (Bormann and Wielandt, 2013). Atmospheric pressure and temperature can generate noise at frequencies below 50 mHz (Bormann and Wielandt, 2013), while wind can generate noise at higher bandwidth between 0.5 to 60 Hz (Bormann and Wielandt, 2013; Withers et al., 1996). Here we observe strong effects of atmospheric signals on the seismic characteristics in the repose time before the magma propagation, and after the eruption. It should be noted that the seismic station FLUR

and the weather station Kárahnjúkar are about 57.9 km apart. While we noticed a shift between the variation of wind speed in comparison with PE, PPE, and IF about 1-2 hours in the hourly window, they can be considered negligible.

Wind speed is found to be strongly correlated with the background noise at frequency higher than 1 Hz (Withers et al., 1996).
315 We observed the strong influence of wind speed on the RMS of the seismic amplitude during the whole repose period (Figures S5h-S12h). Interestingly, we did not observe the influence of wind on PE, PPE, and ~~mean~~-IF in summer. The influence of wind speed on PE, PPE, and ~~mean~~-IF could be seen clearly in spring, especially from February to May (Figures S5 e-g, S9 e-g, S10 e-g) when the fastest wind speed reaches 40 m/s in March 2014, in autumn from September to October (Figure S11 e-g), and in winter (Figure S12 e-g). Wind seems to already influence PE and PPE at the end of the eruption from January to February
320 2015 when the wind speed reaches about 25 m/s and the tremor amplitude is low, while the ~~mean~~-IF is less affected (Figures S8 e-g and S9 e-g). Nevertheless, the wind effects on PE, PPE, and IF are found to be negligible during the magma propagation and the main eruption phase.

During the repose time, PE, PPE, and ~~mean~~-IF show clear daily cycles with high correlations with the temperature changes, as shown in Figure S6 a-c, for the temperatures recorded by the Icelandic Meteorological Office between June and August
325 2014. Similar results are observed for the summer months of 2015 (Figures S10 a-c and S11 a-c). This is surprising because the influence of temperature on seismic wave with frequencies higher than 50 mHz is usually very small and negligible for most seismological processing. For example, it does not seem to influence the temporal variation of the RMS of seismic amplitude for the whole observation period (Figures S5d-S12d). However, PE and PPE depend only on the order of the consecutive values of the amplitude and instantaneous phase, but not on their magnitudes. A very small difference in the consecutive
330 values can change the order and create a different ordinal pattern, hence increasing the calculated entropy. Temperature affects both the thermoelasticity of the seismometer, especially the analyzed vertical component (Bormann and Wielandt, 2013), and the underlying rocks (Prawirodirdjo et al., 2006). However, the temperature effect on PE, PPE, and ~~mean~~-IF are found to be negligible during the magma propagation and the main eruption.

Donaldson et al. (2019) estimate over 10 years variation of relative velocity changes (dv/v) in the crustal rock of central
335 Iceland, including Bárðarbunga and Holuhraun. They observed the dv/v to be high in the winter and spring and low in the summer and fall. This seasonal variation is associated with (i) the changes in the elastic loading on the rocks due to the seasonal changes of snow thickness and the atmospheric pressure, and (ii) the annual variation of the ground water level. They did not compare dv/v with the wind speed and temperature. Wind speed is usually not considered to influence dv/v , while the atmospheric temperature can still affect the dv/v through the thermoelasticity of the crustal rocks (Hillers et al., 2015;
340 Prawirodirdjo et al., 2006). In our two-year observation, we did not observe a clear change due to these long-period seasonal variations. While these seasonal changes in the crustal properties might affect the variation of PE, PPE, and IF, it seems to be much weaker compared to the daily variation due to the atmospheric noise.

5.3 The influence of the magma propagation on PE, PPE, and IF

PE and ~~mean~~-IF increase sharply on 16 August 2014. Both values remain at elevated levels until the onset of the main eruption
345 on 31 August 2014. In contrast, PPE does not increase, but its fluctuation gradually decreases until the main eruption. The high

PE and ~~mean-IF~~ are caused by the high dominant frequencies of earthquakes and their energy distribution in a broad frequency range. We investigated the rotation of their analytic signal in a complex plane (Figure S4b). Compared to ambient noise (Figure S4a), earthquakes exhibit less complex rotation and therefore lower PPE.

PE and ~~mean-IF~~ increase not only at the initial start of the magma propagation (segment S1), but also at the start of other
350 segments, followed by a gentle, gradual decrease towards the end of each segment (Figure 4a,c). Only for S3 does PE not show this pattern, while ~~mean-IF~~ shows it for all segments. This pattern may reflect that the magma propagation in the initial phase of each segment released more fracture energy to open the pathways, and less energy was needed later when the dike only continued to open until the dike extended into another segment (Sigmundsson et al., 2015; Ágústsdóttir et al., 2016, 2019). We checked the distribution of the earthquakes' magnitudes and observed that the magnitudes are mostly ~~smaller at the end~~
355 ~~of the segments~~getting smaller temporally when the segment is ending. However, the RMS signal is too spiky to clearly show the same trend (Figure 4d). An equivalent case is observed in the seismic cycle of tectonic earthquakes, where the Shannon Entropy is found to gradually drop to its initial state after the main shock during the post-seismic states (De Santis et al., 2011; Posadas et al., 2023). Here, the main shock corresponds to the dike migration phase in a segment, and the post-seismic state corresponds to the dike thickening after its extension.

PPE of earthquakes is found to be lower than the PPE of the ambient noise. Its temporal evolution during the earthquake
360 migration exhibits stronger changes than PE. At the beginning of segments S1 to S4, PPE is low and then increases to the end of the segment. As most of the seismic moment is released and more earthquakes are generated at the beginning of each dyke segment, PPE first drops and then increases towards the end of the segment when the number of earthquakes becomes less. During segment S3, PPE did not drop suddenly, but decreased over 2 days until 20 August 2014, before increasing to the
365 end of the segment. An anti-correlated trend is shown by the ~~mean-IF~~, while it increased from 18 to 20 August 2014 before it decreased back to the end of segment S3. From 19 to 23 August 2014, the earthquake migration was reported to stop before changing its direction from south-east to north-east (Sigmundsson et al., 2015).

A single peak of PPE and a drop of ~~mean-IF~~ are observed on 22 August 2014 at 07:00 to 13:00. These are associated with
370 ~~the short period of quiescence during this time~~small earthquakes during these hours. When the S4 dike segment formed, the earthquakes reached the closest distance from FLUR station, which is about 10 km (Figure 4e). These earthquakes dominate the time series, causing PPE to reach the lowest ~~trendpoint~~, while the RMS reaches the highest value (Figure 4d).

After stopping for 81 hours, the dike started to move again and generated segment S4 on 23 August 2014, it was accompanied
375 by a pre-eruptive tremor (Eibl et al., 2017b). This tremor could also be associated with the formation of cauldron C1 which was visually observed on 27 August 2014 (Reynolds et al., 2017). However, this tremor was concealed by a high seismicity rate during the lateral movement of segment S4 (Figure 1). Therefore, it is not seen in PE, PPE and ~~mean-IF~~.

There was a lack of shallow seismicity prior to the eruption (Ágústsdóttir et al., 2019; Eibl et al., 2017b). Following the
380 earthquakes moving horizontally at ~~depth~~depths 5 to 8 km (Ágústsdóttir et al., 2019; Woods et al., 2019), long period (LP) events were detected for about 10 days, starting from 25 August 2014. These LP events had a dominant frequency ~ 1 Hz, clear P and S onset, and occurred at ~ 4 km depth (Woods et al., 2018). Eibl et al. (2017b) suggested the possibility of pre-eruptive tremor that is formed by repetitive microearthquakes at less than 3 km depth followed by silent magma migration to the surface.

However, by utilizing PE, PPE and ~~mean~~-IF, we could not observe any changes that could be related to pre-eruptive tremor before the eruption onsets on 29 and 31 August 2014. The seismic wave generated by earthquakes seems to be dominating the time series, masking other processes, especially during the last dike segment S4, when the earthquakes reach the closest distance to the station, and the changes in PE, PPE, and ~~mean~~-IF become less significant than the earlier segments.

385 Eruption forecasting is easier when the pre-eruptive process generates a pattern of distinct seismic events that are chronologically changing in time and depth. In the case of Strokkur Geyser, the PE variation can characterize the four different phases in the geyser's eruptive cycle (Sudibyó et al., 2022), which are eruption, conduit refilling, gas accumulation in the bubble trap, and the collapses of the bubble ~~gas~~ in the shallow conduit (Eibl et al., 2021). These different processes generate distinct signals with different complexity, thus resulting in distinct values of the corresponding PE. Furthermore, each phase takes
390 place ~~in~~-at separated locations and depths (Eibl et al., 2021). Therefore, not only Sudibyó et al. (2022) can observe a high correlation between PE and the hypocentral distance between seismic event's source and the seismic station, they can also use PE to accurately predict the geyser's eruptions. Konstantinou et al. (2022) reported a consistently decreasing PE prior and during 3 eruptions in Shinmoedake, a stratovolcano in Japan, which is associated ~~to~~-with the dominant occurrence of the pre- and eruptive tremor. In Shinmoedake, as magma moves to ~~the~~-shallower depth and the higher frequency of the seismic events
395 get attenuated, PE drops before the eruption starts. In contrast, the 2014/2015 Holuhraun eruption is preceded by two weeks of lateral dike propagation, dominated by high-frequency events. Changes in the types of seismic events is minor during the pre-eruptive process, and the majority of the events do not move to ~~the~~-shallower depth, causing less significant evolution in the seismic parameters ~~to~~-towards the eruption's onset.

5.4 PE, PPE, and ~~mean~~-IF reflecting the dynamics of eruptive tremor

400 In contrast to the pre-eruptive tremor, the dynamic of the eruptive tremor is well reflected by the properties of PE, PPE, and ~~mean~~-IF. After the main eruption starts, the eruptive tremor dominates the 6 months of eruption, and we observed decreasing values of PE and ~~mean~~-IF, while PPE increases. Volcanic tremors have been reported to have a low PE due to their low dominant frequency and narrow spectral distribution (Konstantinou et al., 2022). The eruptive tremor in Holuhraun has most energy in a low and narrow frequency band ranging from 0.8 to 2.5 Hz (Eibl et al., 2017b). We investigated the seismic analytic wave of
405 the eruptive tremor and found that its rotation is more complex compared to earthquakes (Figure S4d). While the presence of noise could increase the complexity of phase angle rotation, the trend of PPE does not align with the trend of the ambient noise (Figures S7 and S8). Therefore, it is more likely that the calculated PPE represents the characteristics of the eruptive tremor itself.

Eibl et al. (2017a) have identified multiple sources generating the eruptive tremor accompanying the Holuhraun eruption.
410 These sources are associated with fissure locations and the height of the lava fountain, the growth of the lava flow field and intrusions at depth. Hibert et al. (2015) found a linear correlation between seismic energy of tremor with lava effusive rate in Piton de la Fournaise volcano in La Réunion island. Figure 5 shows the comparison of the magma effusive rate estimated by Coppola et al. (2017) with the temporal variation of PE, PPE, ~~mean~~-IF, and seismic root-mean-square (RMeS), where we fitted a horizontal dashed line to the early values of each parameter as a reference and observed decrease of the values with

415 time. Both PE and PPE show an alignment with the magma effusive rate (Figure 5 b and c). Starting from January 2015, PE and PPE start to decline faster, which indicates the eruption is ending. A similar pattern was observed by Sudiby et al. (2022), studying the temporal variation of PE during 63 eruptions of Strokkur Geysir, Iceland. During eruptions with two to four water fountains in quick succession, PE ~~stays stayed~~ high and only ~~drops dropped~~ after the end of the last water fountain of one eruption.

420 On 3 September 2014, a strong tremor was recorded for about 21 hours ~~;(Eibl et al., 2017b; Woods et al., 2018)~~(Eibl et al., 2017b; Woods et al., 2018), which is assumed to have preceded a sub-glacial eruption deepening either the cauldron C2 (Eibl et al., 2017b) or C1 (Woods et al., 2018). We noticed the drop in PE and PPE on 3 September 2014. PE and PPE reach the minimum value at 12:00 for 6 hours before they start increasing back to the previous level at 18:00. The analytic signal shows fewer entangled rotations (Figure S4c) than the main eruption tremor, which is similar to earthquakes (Figure S4b) and causes low PPE. The PE and ~~mean-IF~~ are also low, suggesting that the energy of the tremor is concentrated in a low and narrow frequency band. This result supports Eibl et al. (2017b), who suggested that the tremor is comprised of swarms of microseismicity associated with the fracturing of the shallow crust above the dike.

Woods et al. (2018) observed that the tremor on 3 September has a similar spectral content as the LP swarms which were recorded from 25 August to 2 September 2014. They suggested that the LP swarms could represent magma moving above the
430 dike which culminates in tremor, producing the sub-glacial eruption. As we cannot resolve the LP swarms during the mentioned period, we cannot confirm nor reject their interpretation.

PE, PPE, and ~~mean-IF~~ then undergo a fluctuation from 4 to 7 September 2014 (Figures 4 b and c). This fluctuation could be associated with the opening of two fissures located on the south of the main eruption, resulting in a minor eruption from 5 to 7 September 2014. Thereafter, the PE, PPE, and ~~mean-IF~~ started to be more stable throughout the eruption (Figures 5 a, b and c).

435 5.5 Cluster analysis

~~Based on the chronology information, we plotted~~ Figure 6 compares the clusters generated by the K-means algorithm (panels a-f) and the expert interpretation (panels g-l) using the parameters of PE, PPE, and ~~mean-IF~~ into four clusters: ~~quiescence, dike segment formation-IF, and log(RMeS)~~. Visually they are highly similar, with cluster 1 corresponding to the quiescence, cluster 3 corresponding to the dyke segments S1 to S4, ~~the presumed subglacial eruption, and~~ and cluster 2 corresponding to the subaerial eruption and presumed subglacial eruption. The confusion matrix shows that 96.2% of the data points during quiescence are classified into cluster 1, 96.4% of the data points during dyke propagation are classified into cluster 3, and 86.5% of the data points in the eruption phase are classified into cluster 2 by the K-means algorithm (see Table 1). This score, 86.5%, is the highest score in the eruption cluster in comparison to other clustering results using different combinations (see Table S1 to S4 in the supplementary file). ~~This aims to illuminate whether the different clusters are separated in space or overlap each other. Figure 6 shows a good separation between the clusters. While having a similar trend, the S1 and S2 segments are also separated from S3 and S4 in all plots. This result endorses the potential of PE, PPE, and IF capability to discriminate events and monitor the eruption process.~~

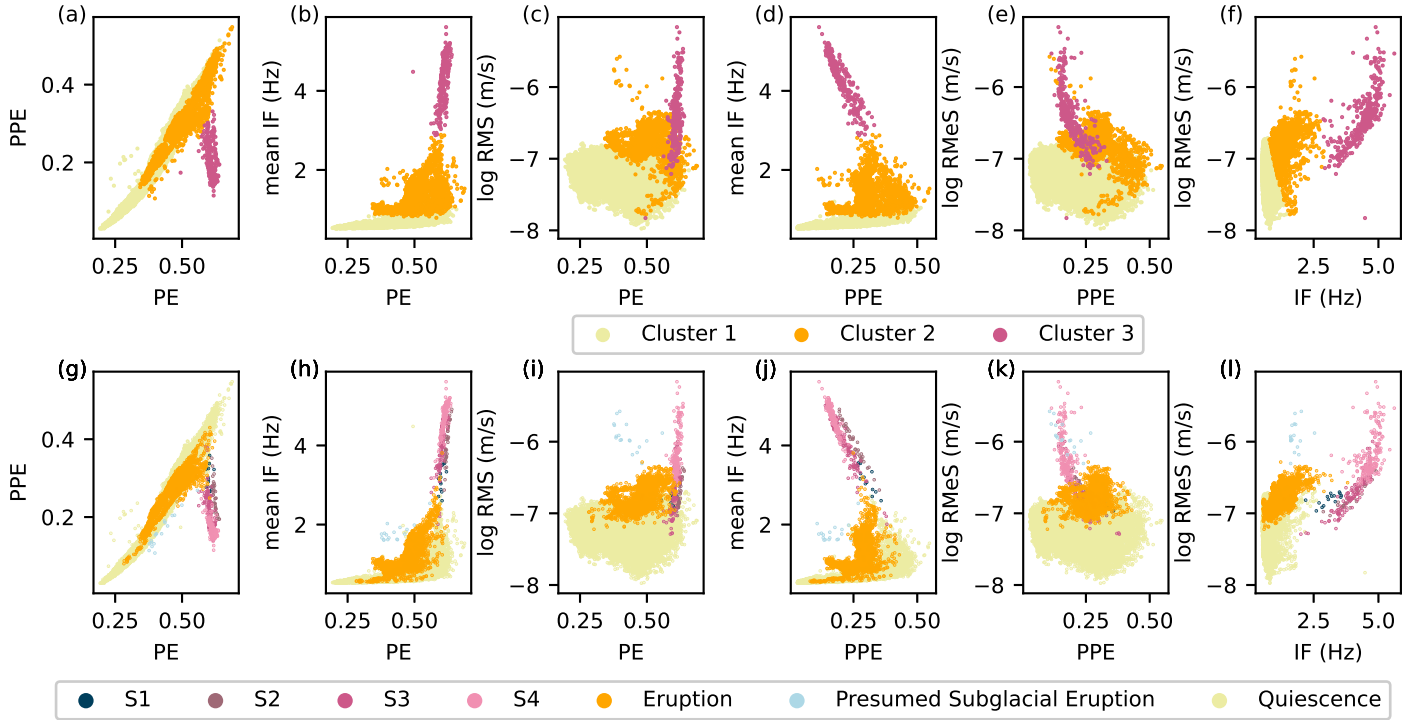


Figure 6. Clustering plots based on the K-means algorithm (aa-f) PPE vs. PE, and an expert interpretation (bg-l) IF vs. using PE, PPE, IF, and $\log(eRMeS)$ IF vs. PPE for the Cluster 1 is associated with quiescence (black), dike cluster 2 is associated with the eruption and presumed subglacial eruption, and cluster 3 is associated with the dyke segments S1 to S4 (blue to dark orange), S2, S3, and the eruption period (orange) S4.

Expert Interpretation \ K-means	Cluster 1	Cluster 2	Cluster 3
	Quiescence	0.962	0.037
Dyke Propagation (S1-S4)	0	0.036	0.964
Eruption and presumed subglacial eruption	0.122	0.865	0.013

Table 1. Confusion matrix between clusters formed by K-means and expert interpretation using PE, PPE, IF, and $\log(RMeS)$ in Figure 6. It shows that 96.2% of the data points during quiescence are classified into cluster 1, 96.4% of the data points during the dyke propagation are classified into cluster 3, and 86.5% of the data points during the eruption and presumed subglacial eruption are classified into cluster 2. The summation of values in each row is equal to 1.

6 Conclusions

In this study, we assessed the capability of PE, PPE, and IF estimated from continuous seismic recordings to characterize the changing state before, during, and after the 2014-2015 Holuhraun eruption in Iceland. ~~by utilizing continuous seismic time series.~~ We observed that temperature and wind ~~influence~~ strongly influence PE and PPE during the repose time, but their effect is minor during the dike migration and eruption. ~~We found that PE, PPE, and IF can resolve the different stages from the repose time followed by~~ Intense volcano-tectonic earthquakes occurred during the dike propagation with high-frequency content, complex amplitude motion, and more regular motion of the instantaneous phase. After the main eruption started, the signal was dominated by volcanic tremor with low-frequency content and more regular amplitude motion but more complex motion of the instantaneous phase. The intense volcano-tectonics earthquakes before the eruption onset complicate the prediction of the eruption onset prior to its occurrence, which could be different when tremor and/or low-frequency events are more dominant.

While prior to the eruption, the changes in IF and PPE were stronger than PE, the variation of PE and PPE became more stable after the eruption started, and their decay indicated the dike propagation through different segments, the multiple eruptions during the eruptive period, and the end of the main eruption. We show that combining these parameters could be a useful tool in discriminating different seismic signals and monitoring their evolution in the time domain. While our study shows that it is still challenging to determine the eruption onset after the start of the pre-eruptive seismicity, PE and PPE have the potential to help predict the duration of the eruption and when the eruption is likely to end. Limiting the analysis using only one or two parameters may not be sufficient as they capture different parts of the eruptive process differently. One parameter can be more sensitive to a certain process than others, and parameter combinations may improve the monitoring of potential changes in a volcanic system. Using clustering analysis, we tested which parameter combination best separates different processes. We found that including $\log(\text{RMes})$ provides more accurate cluster separation than only using PE, PPE, and IF. We did not investigate how the clusters temporarily evolve with respect to different eruption stages or whether there is a sign when the cluster is about to change. Analysing the temporal change in a multi-dimensional space requires different approaches and is reserved for future studies.

Data availability. The seismic waveform data of FLUR and KVER stations are part of Northern Volcanic Zone (NVZ) seismic network installed by the University of Cambridge, United Kingdom. The data is publicly available via the IRIS Data Management Center (IRISDMC).

Author contributions. Conceptualization: MRPS, EPSE, SH; Formal Analysis: MRPS; Funding acquisition: MRPS, EPSE, SH; Investigation: MRPS; Supervision: EPSE, SH; Visualization: MRPS; Writing – original draft preparation: MRPS; Writing – review and editing: MRPS, EPSE, SH, MO

Competing interests. The authors declare that they have no conflict of interest

Acknowledgements. We thank the University of Cambridge which made the seismic data of Northern Volcanic Zone (NVZ) seismic network publicly available. We thank Guðrún Nína Petersen from the Icelandic Meteorological Office ~~for providing the weather catalog~~, who on 19 November ~~2020~~, 2020 provided the weather catalog. This research is funded by DAAD Doctoral Research Grant 57507871. We thank two anonymous reviewers for the useful suggestion in improving this manuscript.

References

- Amigó, J. M., Zambrano, S., and Sanjuán, M. A.: Combinatorial detection of determinism in noisy time series, *Europhysics letters*, 83, 60005, 2008.
- Bandt, C. and Pompe, B.: Permutation Entropy: A Natural Complexity Measure for Time Series, *Physical Review Letters*, 73, 485 <https://doi.org/10.1103/PhysRevLett.88.174102>, 2002.
- Barnes, A. E.: The calculation of instantaneous frequency and instantaneous bandwidth, *Geophysics*, 57, 1520–1524, 1992.
- Berger, S., Schneider, G., Kochs, E. F., and Jordan, D.: Permutation entropy: Too complex a measure for EEG time series?, *Entropy*, 19, 692, 2017.
- Bishop, C. M.: *Pattern Recognition and Machine Learning*, chap. 9. Mixture Models and EM, pp. 423–459, Springer, 2006.
- 490 Boashash, B.: Estimating and interpreting the instantaneous frequency of a signal. I. Fundamentals, *Proceedings of the IEEE*, 80, 520–538, 1992.
- Bormann, P. and Wielandt, E.: *Seismic Signals and Noise*, in: *New Manual of Seismological Observatory Practice 2 (NMSOP2)*, edited by Bormann, P., Deutsches GeoForschungsZentrum GFZ, Potsdam, 2013.
- Bozdağ, E., Trampert, J., and Tromp, J.: Misfit functions for full waveform inversion based on instantaneous phase and envelope measurements, *Geophysical Journal International*, 185, 845–870, 2011.
- 495 Breguier, F., Shapiro, N. M., Campillo, M., Ferrazzini, V., Duputel, Z., Coutant, O., and Nercessian, A.: Towards forecasting volcanic eruptions using seismic noise, *Nature Geoscience*, <https://doi.org/10.1038/ngeo104>, 2008.
- Coppola, D., Laiolo, M., Cigolini, C., Donne, D. D., and Ripepe, M.: Enhanced volcanic hot-spot detection using MODIS IR data: results from the MIROVA system, *Geological Society, London, Special Publications*, 426, 181–205, 2016.
- 500 Coppola, D., Ripepe, M., Laiolo, M., and Cigolini, C.: Modelling satellite-derived magma discharge to explain caldera collapse, *Geology*, 45, 523–526, <https://doi.org/10.1130/G38866.1>, 2017.
- Cropper, W. H.: Rudolf Clausius and the road to entropy, *American journal of physics*, 54, 1068–1074, 1986.
- De Plaen, R. S. M., Lecocq, T., Caudron, C., Ferrazzini, V., and Francis, O.: Single-station monitoring of volcanoes using seismic ambient noise, *Geophysical Research Letters*, 43, 8511–8518, <https://doi.org/10.1002/2016GL070078>, 2016.
- 505 De Plaen, R. S. M., Cannata, A., Cannavo', F., Caudron, C., Lecocq, T., and Francis, O.: Temporal Changes of Seismic Velocity Caused by Volcanic Activity at Mt. Etna Revealed by the Autocorrelation of Ambient Seismic Noise, *Frontiers in Earth Science*, 6, <https://doi.org/10.3389/feart.2018.00251>, 2019.
- De Santis, A., Cianchini, G., Favali, P., Beranzoli, L., and Boschi, E.: The Gutenberg–Richter law and entropy of earthquakes: Two case studies in Central Italy, *Bulletin of the Seismological Society of America*, 101, 1386–1395, 2011.
- 510 Donaldson, C., Winder, T., Caudron, C., and White, R. S.: Crustal seismic velocity responds to a magmatic intrusion and seasonal loading in Iceland's Northern Volcanic Zone, *Science Advances*, 5, eaax6642, 2019.
- Dávalos, A., Jabloun, M., Ravier, P., and Buttelli, O.: The Impact of Linear Filter Preprocessing in the Interpretation of Permutation Entropy, *Entropy*, 23, <https://doi.org/10.3390/e23070787>, 2021.
- Eibl, E. P. S., Bean, C. J., Jónsdóttir, I., Höskuldsson, A., Thordarson, T., Coppola, D., Witt, T., and Walter, T. R.: Multiple coincident eruptive seismic tremor sources during the 2014–2015 eruption at Holuhraun, Iceland, *Journal of Geophysical Research: Solid Earth*, 122, 2972–2987, <https://doi.org/10.1002/2016JB013892>, 2017a.
- 515

- Eibl, E. P. S., Bean, C. J., Vogfjörð, K. S., Ying, Y., Lokmer, I., Möllhoff, M., O'Brien, G. S., and Pálsson, F.: Tremor-rich shallow dyke formation followed by silent magma flow at Bárðarbunga in Iceland, *Nature Geoscience*, 10, 299–304, <https://doi.org/10.1038/ngeo2906>, 2017b.
- 520 Eibl, E. P. S., Hainzl, S., Vesely, N. I., Walter, T. R., Jousset, P., Hersir, G. P., and Dahm, T.: Eruption interval monitoring at Strokkur geysir, Iceland, *Geophysical Research Letters*, 47, e2019GL085266, 2020.
- Eibl, E. P. S., Müller, D., Walter, T. R., Allahbakhshi, M., Jousset, P., Hersir, G. P., and Dahm, T.: Eruptive Cycle and Bubble Trap of Strokkur Geysir, Iceland, *Journal of Geophysical Research: Solid Earth*, 126, e2020JB020769, <https://doi.org/10.1029/2020JB020769>, 2021.
- Feldman, M.: Hilbert transform in vibration analysis, *Mechanical systems and signal processing*, 25, 735–802, 2011.
- 525 Gabor, D.: Theory of communication. Part I: The analysis of information, *Journal of the Institution of Electrical Engineers-part III: radio and communication engineering*, 93, 429–441, 1946.
- Glynn, C. C. and Konstantinou, K. I.: Reduction of randomness in seismic noise as a short-term precursor to a volcanic eruption, *Scientific Reports*, 6, 37733, <https://doi.org/10.1038/srep37733>, 2016.
- Harris, C. R., Millman, K. J., van der Walt, S. J., Gommers, R., Virtanen, P., Cournapeau, D., Wieser, E., Taylor, J., Berg, S., Smith, N. J.,
530 Kern, R., Picus, M., Hoyer, S., van Kerkwijk, M. H., Brett, M., Haldane, A., del Río, J. F., Wiebe, M., Peterson, P., Gérard-Marchant, P., Sheppard, K., Reddy, T., Weckesser, W., Abbasi, H., Gohlke, C., and Oliphant, T. E.: Array programming with NumPy, *Nature*, 585, 357–362, <https://doi.org/10.1038/s41586-020-2649-2>, 2020.
- Hibert, C., Mangeney, A., Polacci, M., Muro, A. D., Vergnolle, S., Ferrazzini, V., Peltier, A., Taisne, B., Burton, M., Dewez, T., Grandjean, G., Dupont, A., Staudacher, T., Brenguier, F., Kowalski, P., Boissier, P., Catherine, P., and Lauret, F.: Toward continuous quantification
535 of lava extrusion rate: Results from the multidisciplinary analysis of the 2 January 2010 eruption of Piton de la Fournaise volcano, La Réunion, *Journal of Geophysical Research: Solid Earth*, 120, 3026–3047, <https://doi.org/10.1002/2014JB011769>, 2015.
- Hillers, G., Ben-Zion, Y., Campillo, M., and Zigone, D.: Seasonal variations of seismic velocities in the San Jacinto fault area observed with ambient seismic noise, *Geophysical Journal International*, 202, 920–932, <https://doi.org/10.1093/gji/ggv151>, 2015.
- Illien, L., Sens-Schönfelder, C., and Ke, K.-Y.: Resolving minute temporal seismic velocity changes induced by earthquake damage: the
540 more stations, the merrier?, *Geophysical Journal International*, 234, 124–135, 2023.
- Kang, H., Zhang, X., and Zhang, G.: Phase permutation entropy: A complexity measure for nonlinear time series incorporating phase information, *Physica A: Statistical Mechanics and its Applications*, 568, 125686, <https://doi.org/10.1016/j.physa.2020.125686>, 2021.
- Konstantinou, K. I., Rahmalia, D. A., Nurfitriana, I., and Ichihara, M.: Permutation entropy variations in seismic noise before and after eruptive activity at Shinmoedake volcano, Kirishima complex, Japan, *Earth, Planets and Space*, <https://doi.org/10.1186/s40623-022-01729-9>,
545 2022.
- Moran, S. C., Freymueller, J. T., LaHusen, R. G., McGee, K. A., Poland, M. P., Power, J. A., Schmidt, D. A., Schneider, D. J., Stephens, G., Werner, C. A., et al.: Instrumentation recommendations for volcano monitoring at US volcanoes under the National Volcano Early Warning System, *US Geological Survey Scientific Investigations Report*, 5114, 47, 2008.
- Pedersen, G., Höskuldsson, A., Dürig, T., Thordarson, T., Jonsdóttir, I., Riishuus, M., Óskarsson, B., Dumont, S., Magnússon, E., Gudmundsson, M. T., et al.: Lava field evolution and emplacement dynamics of the 2014–2015 basaltic fissure eruption at Holuhraun, Iceland,
550 *Journal of Volcanology and Geothermal Research*, 340, 155–169, 2017.
- Pedregosa, F., Varoquaux, G., Gramfort, A., Michel, V., Thirion, B., Grisel, O., Blondel, M., Prettenhofer, P., Weiss, R., Dubourg, V., Vanderplas, J., Passos, A., Cournapeau, D., Brucher, M., Perrot, M., and Duchesnay, E.: Scikit-learn: Machine Learning in Python, *Journal of Machine Learning Research*, 12, 2825–2830, 2011.

- 555 Posadas, A., Morales, J., Ibañez, J., and Posadas-Garzon, A.: Shaking earth: Non-linear seismic processes and the second law of thermodynamics: A case study from Canterbury (New Zealand) earthquakes, *Chaos, Solitons & Fractals*, 151, 111 243, 2021.
- Posadas, A., Pasten, D., Vogel, E. E., and Saravia, G.: Earthquake hazard characterization by using entropy: application to northern Chilean earthquakes, *Natural Hazards and Earth System Sciences*, 23, 1911–1920, <https://doi.org/10.5194/nhess-23-1911-2023>, 2023.
- Prawirodirdjo, L., Ben-Zion, Y., and Bock, Y.: Observation and modeling of thermoelastic strain in Southern California Integrated GPS
560 Network daily position time series, *Journal of Geophysical Research: Solid Earth*, 111, <https://doi.org/10.1029/2005JB003716>, 2006.
- Reynolds, H. I., Gudmundsson, M. T., Högnadóttir, T., Magnússon, E., and Pálsson, F.: Subglacial volcanic activity above a lateral dyke path during the 2014–2015 Bárðarbunga-Holuhraun rifting episode, Iceland, *Bulletin of Volcanology*, 79, <https://doi.org/10.1007/s00445-017-1122-z>, 2017.
- Saccorotti, G. and Lokmer, I.: A review of seismic methods for monitoring and understanding active volcanoes, *Forecasting and planning for*
565 *volcanic hazards, risks, and disasters*, pp. 25–73, 2021.
- Schimmel, M., Stutzmann, E., and Gallart, J.: Using instantaneous phase coherence for signal extraction from ambient noise data at a local to a global scale, *Geophysical Journal International*, 184, 494–506, 2011.
- Sens-Schönfelder, C. and Wegler, U.: Passive image interferometry and seasonal variations of seismic velocities at Merapi Volcano, Indonesia, *Geophysical Research Letters*, 33, <https://doi.org/10.1029/2006GL027797>, 2006.
- 570 Shannon, C. E.: A mathematical theory of communication, *The Bell system technical journal*, 27, 379–423, 1948.
- Sigmundsson, F., Hooper, A., Hreinsdóttir, S., Vogfjörð, K. S., Ófeigsson, B. G., Heimisson, E. R., Dumont, S., Parks, M., Spaans, K., Gudmundsson, G. B., Drouin, V., Árnadóttir, T., Jónsdóttir, K., Gudmundsson, M. T., Högnadóttir, T., Fridriksdóttir, H. M., Hensch, M., Einarsson, P., Magnússon, E., Samsonov, S., Brandsdóttir, B., White, R. S., Ágústsdóttir, T., Greenfield, T., Green, R. G., Hjartardóttir, A. R., Pedersen, R., Bennett, R. A., Geirsson, H., La Femina, P. C., Björnsson, H., Pálsson, F., Sturkell, E., Bean, C. J., Möllhoff, M.,
575 Braiden, A. K., and Eibl, E. P. S.: Segmented lateral dyke growth in a rifting event at Bárðarbunga volcanic system, Iceland, *Nature*, 517, 191–195, <https://doi.org/10.1038/nature14111>, 2015.
- Steinmann, R., Hadziioannou, C., and Larose, E.: Effect of centimetric freezing of the near subsurface on Rayleigh and Love wave velocity in ambient seismic noise correlations, *Geophysical Journal International*, 224, 626–636, <https://doi.org/10.1093/gji/ggaa406>, 2020.
- Sudibyo, M. R. P., Eibl, E. P. S., Hainzl, S., and Hersir, G. P.: Eruption Forecasting of Strokkur Geyser, Iceland, Using Permutation
580 Entropy, *Journal of Geophysical Research: Solid Earth*, 127, e2022JB024 840, <https://doi.org/10.1029/2022JB024840>, e2022JB024840 2022JB024840, 2022.
- Taner, M. T., Koehler, F., and Sheriff, R. E.: Complex seismic trace analysis, *GEOPHYSICS*, 44, 1041–1063, <https://doi.org/10.1190/1.1440994>, 1979.
- Thompson, G., Beer, M., Kougioumtzoglou, I., Patelli, E., and Au, S.: Seismic monitoring of volcanoes, *Encyclopedia of earthquake engineering*, 10, 1–25, 2015.
585
- Virtanen, P., Gommers, R., Oliphant, T. E., Haberland, M., Reddy, T., Cournapeau, D., Burovski, E., Peterson, P., Weckesser, W., Bright, J., van der Walt, S. J., Brett, M., Wilson, J., Millman, K. J., Mayorov, N., Nelson, A. R. J., Jones, E., Kern, R., Larson, E., Carey, C. J., Polat, Í., Feng, Y., Moore, E. W., VanderPlas, J., Laxalde, D., Perktold, J., Cimrman, R., Henriksen, I., Quintero, E. A., Harris, C. R., Archibald, A. M., Ribeiro, A. H., Pedregosa, F., van Mulbregt, P., and SciPy 1.0 Contributors: SciPy 1.0: Fundamental Algorithms for Scientific
590 Computing in Python, *Nature Methods*, 17, 261–272, <https://doi.org/10.1038/s41592-019-0686-2>, 2020.
- Voigt, J. R., Hamilton, C. W., Scheidt, S. P., Münzer, U., Höskuldsson, Á., Jónsdóttir, I., and Thordarson, T.: Geomorphological characterization of the 2014–2015 Holuhraun lava flow-field in Iceland, *Journal of Volcanology and Geothermal Research*, 419, 107 278, 2021.

- Wassermann, J.: Volcano Seismology, in: *New Manual of Seismological Observatory Practice 2 (NMSOP2)*, Deutsches GeoForschungsZentrum GFZ, Potsdam, https://doi.org/10.2312/GFZ.NMSOP-2_ch13, 2012.
- 595 Wehrl, A.: General properties of entropy, *Reviews of Modern Physics*, 50, 221, 1978.
- White, R.: Northern Volcanic Zone, International Federation of Digital Seismograph Networks, https://www.fdsn.org/networks/detail/Z7_2010/, 2010.
- Withers, M. M., Aster, R. C., Young, C. J., and Chael, E. P.: High-frequency analysis of seismic background noise as a function of wind speed and shallow depth, *Bulletin of the Seismological Society of America*, 86, 1507–1515, <https://doi.org/10.1785/BSSA0860051507>,
600 1996.
- Woods, J., Donaldson, C., White, R. S., Caudron, C., Brandsdóttir, B., Hudson, T. S., and Ágústsdóttir, T.: Long-period seismicity reveals magma pathways above a laterally propagating dyke during the 2014–15 Bárðarbunga rifting event, Iceland, *Earth and Planetary Science Letters*, 490, 216–229, <https://doi.org/10.1016/j.epsl.2018.03.020>, 2018.
- Woods, J., Winder, T., White, R. S., and Brandsdóttir, B.: Evolution of a lateral dike intrusion revealed by relatively-relocated dike-
605 induced earthquakes: The 2014–15 Bárðarbunga–Holuhraun rifting event, Iceland, *Earth and Planetary Science Letters*, 506, 53–63, <https://doi.org/10.1016/j.epsl.2018.10.032>, 2019.
- Ágústsdóttir, T., Woods, J., Greenfield, T., Green, R. G., White, R. S., Winder, T., Brandsdóttir, B., Steinhórsson, S., and Soosalu, H.: Strike-slip faulting during the 2014 Bárðarbunga–Holuhraun dike intrusion, central Iceland, *Geophysical Research Letters*, 43, 1495–1503, <https://doi.org/10.1002/2015GL067423>, 2016.
- 610 Ágústsdóttir, T., Winder, T., Woods, J., White, R. S., Greenfield, T., and Brandsdóttir, B.: Intense Seismicity During the 2014–2015 Bárðarbunga–Holuhraun Rifting Event, Iceland, Reveals the Nature of Dike-Induced Earthquakes and Caldera Collapse Mechanisms, *Journal of Geophysical Research: Solid Earth*, 124, 8331–8357, <https://doi.org/10.1029/2018JB016010>, 2019.